

Optically faint X-ray sources in the Chandra deep field North: *Spitzer* constraints

E. Rovilos¹, I. Georgantopoulos^{2,3}, A. Akylas³, and S. Fotopoulou^{4,5}

¹ Max-Planck-Institut für Extraterrestrische Physik, Giessenbachstraße, 85748 Garching, Germany
e-mail: erovilos@mpe.mpg.de

² Osservatorio Astronomico di Bologna/INAF, via Ranzani 1, 40127 Bologna, Italy

³ Institute of Astronomy and Astrophysics, National Observatory of Athens, I. Metaxa & V. Pavlou str., Palaia Penteli, 15236 Athens, Greece

⁴ Max-Planck-Institut für Plasmaphysik, Boltzmannstraße 2, 85748 Garching, Germany

⁵ Technische Universität München, Fakultät für Physik, James-Frank-Straße, 85748 Garching, Germany

Received 1 February 2010 / Accepted 2 June 2010

ABSTRACT

We investigate the properties of the most optically faint sources in the GOODS-N area ($R_{AB} > 26.5$). These extremely optically faint populations present an uncharted territory although they represent an appreciable fraction of the X-ray sources in the GOODS-N field. The optically faint sources are believed to contain either red active galactic nuclei (AGN) at moderate redshifts or possibly quasi stellar objects (QSOs) at very high redshift. We compile our sample by first finding the $3.6 \mu\text{m}$ IRAC counterparts of the X-ray sources and in turn by searching for the optical counterparts of the IRAC sources. No counterparts were found for 35 objects in the *R*-band Subaru optical images. Of these, 18 have *HST* ACS counterparts, while the remaining have no optical counterparts. The vast majority of our 35 sources are classified as extremely red objects (EROs) on the basis of their $V_{606} - K_s$ lower limits. Their derived photometric redshifts show that these populate moderate redshifts (median $z \sim 2.8$), being at markedly different redshifts from the already spectroscopically identified population which peaks at $z \sim 0.7$. The *Spitzer* IRAC mid-IR colours of the sources without *HST* counterparts tend to lie within the mid-IR colour diagram AGN “wedge”, suggesting either QSO, ultra luminous infrared galaxy (ULIRG; Mrk231) templates or early-type galaxy templates at $z > 3$. A large fraction of our sources (17/35), regardless of whether they have *HST* counterparts, can be classified as mid-IR bright/optically faint sources (dust obscured galaxies) a class of sources which is believed to include many heavily absorbed AGN. The co-added X-ray spectrum of the optically faint sources is very flat, with a spectral index of $\Gamma \approx 0.87$, significantly flatter than the spectrum of the X-ray background. The optically faint ($R > 26.5$) X-ray sources constitute more than 50 per cent of the total X-ray population at redshifts $z > 2$, bearing important implications for the luminosity function and its evolution. Considering X-ray sources with $2 < z < 4$ we find good agreement with a modified pure luminosity evolution (PLE) model.

Key words. galaxies: active – galaxies: high-redshift – X-rays: galaxies – infrared: galaxies

1. Introduction

X-ray surveys provide the most efficient method for detecting active galactic nuclei (AGN; Brandt & Hasinger 2005). This is because X-ray wavelengths can penetrate a substantial amount of interstellar gas and reveal the AGN even in very obscured systems. The deepest X-ray surveys to date detect a large number of sources down to a flux of $\sim 2 \times 10^{-17} \text{ erg cm}^{-2} \text{ s}^{-1}$ in the (0.5–2.0) keV band (Alexander et al. 2003; Luo et al. 2008). The vast majority of them are AGN (Bauer et al. 2004) with a surface density of about 5000 sources per square degree. Optical follow-up observations have identified a considerable fraction of them (Barger et al. 2003a; Capak et al. 2004; Trouille et al. 2008), revealing that the peak of the redshift distribution based on spectroscopic identifications is at $z = 0.7$. However, a large number of the X-ray sources remain optically unidentified, which hampers our understanding of their nature. In particular, a significant fraction of faint X-ray sources (~50%) lacks a spectroscopic identification (e.g. Luo et al. 2010) and the redshift estimate is made with photometric techniques. Still, Aird et al. (2010) estimate that about one third of the X-ray sources in the *Chandra* deep fields (CDFs) do not have optical counterparts down to $R_{AB} \approx 26.5$.

The nature of these optically faint sources remains puzzling. Two interesting scenarii have been proposed to explain their nature. First, the very faint optical emission could be the result of copious dust absorption; in the CDFs the majority of high f_x/f_o sources shows clear evidence of obscuration in their individual and stacked X-ray spectra (Civano et al. 2005), a result which confirms previous findings (Alexander et al. 2001). On the other hand, a very faint, or the lack of an optical counterpart could indicate a very high redshift source (Koekemoer et al. 2004). In this case, the reason of a high X-ray-to-optical ratio is that the optical bands are probing bluer rest-frame wavelengths, which are more obscured or intrinsically fainter if they fall blueward from the Lyman break. At the same time the observed X-ray wavelengths correspond to high energy rest-frame wavelengths, which are less prone to absorption. Lehmer et al. (2005) used a Lyman break technique to select high-redshift galaxies in the *Chandra* deep fields and found 11 B_{435} , V_{606} , and i_{775} dropouts among the X-ray sources, with possible redshifts $z \gtrsim 4$.

A crucial diagnostic for the nature of optically faint galaxies is their infrared emission. The optical and ultra-violet light that is absorbed is re-emitted in infrared wavelengths, therefore a high infrared-to-optical ratio can be used as a criterion of high obscuration. For example, Houck et al. (2005) discovered a number of sources with extremely high 24 μm to optical

luminosities (see also [Daddi et al. 2007](#)). These sources, nicknamed DOGs (dust obscured galaxies) are located at $1.5 \lesssim z \lesssim 2$ ([Pope et al. 2008](#)). A large fraction of them is probably associated with Compton-thick quasi stellar objects (QSOs; [Fiore et al. 2008, 2009](#); [Treister et al. 2009](#); [Georgantopoulos et al. 2008](#)).

In this paper we explore the properties of optically faint ($R_{AB} \gtrsim 26.5$) X-ray sources in the GOODS-N area. Previous studies of some of the optically faint sources in this field have been performed in the past; [Alexander et al. \(2001\)](#) studied the “brightest” optically faint sources (with $I > 24$) and [Civano et al. \(2005\)](#) investigated the properties of extreme X-ray objects (EXOs), which have an X-ray-to-optical flux ratio > 10 . Instead, our sample focuses not only on EXOs but on all optically faint sources. Additionally, we take advantage of the full 2 Ms X-ray exposures, but more importantly we make use of the mid-IR *Spitzer* observations in order to find the true counterparts of the X-ray sources. We perform anew the search for optical identifications of the X-ray sources in two steps. First, we cross-correlate the X-ray positions with the *Spitzer* IRAC $3.6 \mu\text{m}$ catalogue using a likelihood ratio technique. Then we cross-correlate the IRAC positions with the [Capak et al. \(2004\)](#) *R*-band optical observations. We define the optically faint sources as those with $R_{AB} \gtrsim 26.5$, i.e. beyond the flux limit of this catalogue. Then we look for optical counterparts in the fainter *HST* observations. After deriving photometric redshifts (Sect. 4) we study their X-ray (Sect. 5) as well as their optical and mid-IR properties (Sects. 6 and 7).

2. X-ray, optical, and IR data and counterpart association

We use the 2 Ms CDFN catalogue of [Alexander et al. \(2003\)](#), with a sensitivity of $2.5 \times 10^{-17} \text{ erg cm}^{-2} \text{ s}^{-1}$ in the 0.5–2.0 keV band and $1.4 \times 10^{-16} \text{ erg cm}^{-2} \text{ s}^{-1}$ in the 2.0–8.0 keV band. The infrared (*Spitzer*) data come from the *Spitzer*-GOODS legacy programme ([Dickinson 2004](#)). This includes observations in the mid-infrared with IRAC and MIPS which cover most of the *Chandra* deep field North (CDFN) area. Typical sensitivities of these observations are $0.3 \mu\text{Jy}$ and $80 \mu\text{Jy}$ for the IRAC- $3.6 \mu\text{m}$ and MIPS- $24 \mu\text{m}$ bands respectively. Optical coverage of the GOODS-North field is available both with ground-based (Subaru-SuprimeCam) and space observations (*HST*-ACS). The Subaru sensitivity is 26.5 mag(AB) in the *R* band ([Capak et al. 2004](#)) and the *HST* is 27.8 mag(AB) in the z_{850} band ([Giavalisco et al. 2004](#)). We also make use of near-infrared (K_S -band) observations with Subaru-MOIRCS, reaching a limit of 23.8 mag(AB) ([Bundy et al. 2009](#)).

The X-ray catalogue ([Alexander et al. 2003](#)) has 503 sources detected in one of the hard (2.0–10.0 keV), soft (0.5–2.0 keV), or full (0.5–10.0 keV) bands. Of these sources, 348 fall into the region covered by the IRAC observations. We made an initial simple cross-correlation of the positions of the sources of the two catalogues to check their relative astrometry. We found good agreement in the RA axis ($\langle \text{RA}(\text{Xray}) - \text{RA}(\text{IR}) \rangle = -0.05$, $\sigma = 0.31$), but there is a significant difference in the astrometry in the Dec axis ($\langle \text{Dec}(\text{Xray}) - \text{Dec}(\text{IR}) \rangle = -0.29$, $\sigma = 0.35$, see Fig. 1); we updated the positions of the IR sources accordingly before proceeding to the search of IR counterparts to the X-ray sources.

We used the “likelihood ratio” method ([Sutherland & Saunders 1992](#)) to find the counterparts: we calculated the

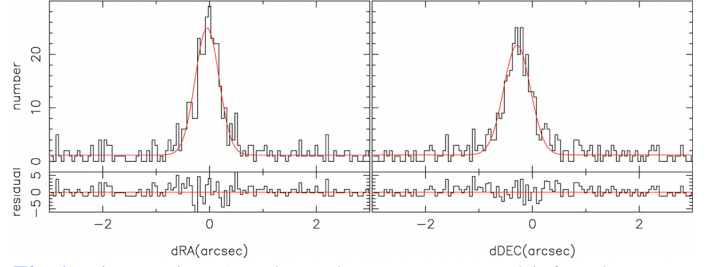


Fig. 1. Distance in RA and Dec between X-ray and infrared sources. There is a significant shift in declination between the two catalogues which we correct for before making the correlation. (This figure is available in color in electronic form.)

likelihood ratio (LR) of an infrared source to be a real counterpart of an X-ray source as

$$LR = \frac{q(m)f(x, y)}{n(m)},$$

where $q(m)$ is the expected magnitude distribution of real counterparts, $f(x, y)$ is the probability distribution function of positional errors, a Gaussian in this case, and $n(m)$ is the magnitude distribution of background objects. We calculate the $q(m)$ function by subtracting the magnitude distribution of the background (IR) sources we expect to find within the search radius near the target (X-ray) sources from the magnitude distribution of all the initial counterparts. The normalization of $q(m)$ is done using

$$\int_{-\infty}^{M_{\text{lim}}} q(m) dm = Q(M_{\text{lim}}),$$

where $Q(M_{\text{lim}})$ is the probability that the IR counterpart is brighter than the magnitude limit M_{lim} ; in practice it is the final fraction of X-ray sources with an IR counterpart. Given that the positional offsets of the X-ray sources in the CDFN at large off-axis angles can be as large as $1''$ – $2''$ ([Alexander et al. 2003](#)), we use a large initial search radius for the X-ray – IR counterparts ($4''$).

The choice of an optimum likelihood ratio cutoff is a compromise between the reliability of the final sample and its completeness. The reliability of a possible counterpart is defined as

$$R_i = \frac{LR_i}{\sum LR_j + (1 - Q(M_{\text{lim}}))},$$

where j refers to the different IR counterparts to a specific X-ray source. We chose the likelihood-ratio cutoff, which maximizes the sum of completeness and reliability of the matched catalogue in the same manner as [Luo et al. \(2010\)](#). The completeness is defined as the ratio of the sum of the reliabilities of the counterparts with $LR > LR_{\text{lim}}$ with the number of the X-ray sources in the area mapped by IRAC, and the reliability is defined as the mean reliability of counterparts with $LR > LR_{\text{lim}}$. In the X-ray – IR case $LR_{\text{lim}} = 0.15$, which gives a reliability of 99.2%.

We detected 330 IR counterparts with $LR > 0.15$, then visually inspected the positions on the IRAC images of the X-ray sources lacking a counterpart and found 12 cases where the IR source is clearly visible but blended with a nearby source in a way that the source extraction algorithm could not distinguish them. Adding these cases, the final number of counterparts is 342 out of the 348 X-ray sources in the IRAC area. Assuming that 0.8% of the counterparts are spurious, the final efficiency is 97.5%.

In order to look for optical counterparts to the X-ray sources we used the positions of their IR counterparts. The positional accuracy of IRAC is better than that of *Chandra*, moreover the NIR

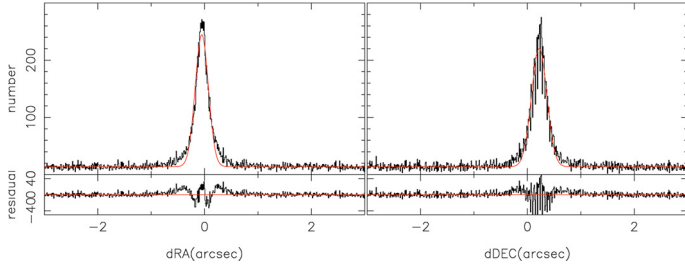


Fig. 2. Same as Fig. 1 but for the *Spitzer* (without including the correction introduced to match the X-ray astrometry) and optical catalogues. The shift in declination is again corrected for before correlating. (This figure is available in color in electronic form.)

is more efficient in detecting AGN than the optical emission, due to the reprocessing of the ionizing radiation of the AGN through circumnuclear and interstellar dust to IR wavelengths. As a result, the efficiency of IRAC in finding counterparts for the X-ray sources (97.5%) is higher than that of the optical survey (78.1% if we follow the procedure described above for the Subaru-*R* catalogue), in spite of the optical being deeper than IRAC (see also Luo et al. 2010, for the CDFS case).

The optical catalogue of Capak et al. (2004) has 47 450 sources detected in the *R* band, and of those 14 763 fall into the area sampled by IRAC. Before searching for optical counterparts, we again checked the relative astrometry of the optical and (uncorrected) IR catalogues. We again found a similar astrometry difference in the Dec axis ($\langle \text{Dec}(\text{opt}) - \text{Dec}(\text{IR}) \rangle = -0.22$, $\sigma = 0.20$, Fig. 2), while the RA positions are well within the error ($\langle \text{RA}(\text{opt}) - \text{RA}(\text{IR}) \rangle = 0.05$, $\sigma = 0.17$). We again corrected the IR catalogue to match the optical positions.

We used the likelihood ratio method to select the optical counterparts to the IR sources. Given the smaller PSF of the optical images we use a smaller initial search radius (3'') and followed the same procedure to select the optimum likelihood-ratio limit. With $LR_{\text{lim}} = 0.25$, which this time gives a mean reliability of 98.4%, we found optical counterparts for 8437 of the 10 595 IRAC sources. The recovery rate is 78.0%. We also performed an independent search for optical counterparts of X-ray sources which do not have an infrared counterpart, or where the latter is a blended source as described above, and found a secure optical counterpart for 12 such cases; 11/12 of the ‘‘confused’’ IR sources have an optical source related to the X-ray position, while 1/6 of the IRAC non-detections is detected in optical. Finally, we optically inspected the Subaru *R*-band images of X-ray sources lacking an optical counterpart and found that in 17 the optical counterpart is clearly visible but without identification in the catalogue of Capak et al. (2004). Two common reasons for that are that the source is saturated, and therefore it does not have reliable photometry, and that it lies close to a very bright source and therefore it is not detected by the source-extracting algorithm.

The X-ray, optical, and infrared properties of all the sources of the common CDFN-IRAC area can be found in ftp.mpe.mpg.de/people/erovilos/CDFN_IR_OPT/

3. Sample selection

In this study we are interested in X-ray sources which are too faint to be detected by typical ground-based optical surveys, like that of Capak et al. (2004). These sources represent a sizable fraction of the overall X-ray population ($\sim 15\%$). They are generally not covered by spectroscopic surveys, which are typically

magnitude-limited with $R_{\text{lim}} < 26.5$ and often do not even have photometric redshifts. Such cases have been studied before in detail (e.g. Alexander et al. 2001; Mainieri et al. 2005); here we approach them using their infrared properties and X-ray spectra.

There are 310 X-ray sources within the common area of all the surveys used in this study (2 Ms CDFN – Subaru-Suprime(optical) – Subaru-MOIRCS(*HK'*) – GOODS-ACS – GOODS-IRAC – GOODS-MIPS). Of these 310 sources, 42 are too faint to be detected in the *R*-band by Subaru-Suprime and are assumed to have $R_{\text{AB}} > 26.5$. No *R*-detected CDFN source has $R_{\text{AB}} > 26.5$. Because we base this study on the infrared properties to examine the nature of optically faint sources, we excluded 7 of the 42 sources from our studied sample for the following reasons: 5 are not detected with IRAC, and 2 are blended with nearby sources, so their infrared photometry is not reliable. Our final sample consists of 35 sources, whose X-ray, optical, and infrared properties are listed in Table 1. Among these sources we expect a mean number of 0.35 spurious encounters (practically none), as the mean reliability of the IRAC counterparts for these 35 cases is 99.0%.

For these 35 sources we searched the K_S catalogue of Bundy et al. (2009) for counterparts. These Subaru-MOIRCS images cover an area slightly smaller than IRAC, and we limited our field to the common area. As the number of sources is small, we looked for K_S -band counterparts by eye; this way we can easily distinguish any K_S -band sources that are physically related to a nearby IRAC source. We found a K_S counterpart for 29/35 sources; their distances from the IRAC sources are all $< 1.4''$, while for the 6 non-detections the distance of the nearest K_S source is always $> 3.9''$. We then searched the *HK'*-band images from the UH-2.2 m telescope (Capak et al. 2004) to detect any sources bright enough in the *HK'* band but not detected in *R*. Using *sextractor* (Bertin & Arnouts 1996), we identify as a source 4 adjacent pixels with fluxes above 1.2 times the local background rms. We find an *HK'* detection for 19 of the sources in our sample. The Subaru-MOIRCS area has very deep optical imaging with the *HST*-ACS as part of the GOODS survey. The catalogues (Giavalisco et al. 2004) are based on detections in the z_{850} band and are publicly available. We searched the sources of our sample for *HST* counterparts using the likelihood-ratio method, as described in the previous section, with an initial search radius of 1.5 arcsec. We use this method because the PSFs of *Spitzer*-IRAC and *HST*-ACS are different within a large factor and there could be multiple ACS sources within one IRAC beam. Of our sample 18/35 sources have an *HST*-ACS counterpart.

We note here that some of the sources in Table 1 appear with full optical photometry in Barger et al. (2003a), some of them even with a photometric redshift. Where X-ray sources lack an optical counterpart, like the those in Table 1, Barger et al. (2003a) measured the optical fluxes directly from the Subaru images using a 3'' diameter aperture centred on the position of the X-ray source. In doing so there is a high probability that light from a neighbouring source enters the aperture, moreover centering on the X-ray positions causes a loss in positional accuracy, which is essential when measuring the flux of a ‘‘non-visible’’ source. Figure 3 shows the *R*-band images of the 35 sources of Table 1, with 4''-radii circles on the X-ray positions (as large as the initial search radius) as well as contours representing the IRAC flux. We can see that in some cases the X-ray and IRAC positions differ significantly and that the 1.5'' aperture centred on the X-ray position would often be contaminated by nearby optical sources.

The sample presented in Table 1 has both similarities and differences with the high X-ray-to-optical ratio sample

Table 1. List of CDFN X-ray sources that are correlated with a *Spitzer* 3.6 μm detection and lack an optical counterpart in Capak et al. (2004).

A03	$f_{(0.5-8.0)}$ keV erg cm ⁻² s ⁻¹	RA (IRAC) deg	Dec (IRAC) deg	B_{435} AB	V_{606} AB	i_{775} AB	z_{850} AB	HK' mag AB	K_s mag Vega	$f_{3.6 \mu\text{m}}$ μJy	$f_{4.5 \mu\text{m}}$ μJy	$f_{5.8 \mu\text{m}}$ μJy	$f_{8.0 \mu\text{m}}$ μJy	$f_{24 \mu\text{m}}$ μJy	$\log \frac{f_x}{f_{V_{606}}}$	z -phot
73	3.65e-15	189.023735	62.144111	>29.443	27.668	26.830	27.138	22.430	22.279	6.677	8.981	12.283	15.299	<56.234	1.75	2.66
84	2.46e-16	189.035878	62.243257	–	–	–	>27.800	–	21.942	6.546	9.558	13.491	17.813	<56.234	>0.63	4.50
98	2.04e-15	189.054272	62.206709	–	–	–	>27.800	–	21.806	5.307	6.999	9.587	9.260	69.975	>1.55	2.76
100	9.39e-16	189.058928	62.171695	–	–	–	>27.800	–	>21.693	2.293	3.458	4.470	7.094	39.019	>1.21	3.95
107	1.77e-15	189.065954	62.254337	–	–	–	>27.800	21.842	20.805	15.406	19.171	25.913	<3.548	<56.234	>1.49	3.13
125	2.27e-16	189.088021	62.217674	27.885	27.687	26.960	26.218	21.569	21.479	8.205	9.576	13.275	10.552	<56.234	0.55	1.58
129	1.22e-15	189.091308	62.267668	>30.195	30.080	>29.676	28.734	21.938	20.930	10.754	13.262	14.610	10.325	104.577	2.24	2.78
140	5.45e-16	189.098728	62.169285	–	–	–	>27.800	22.355	21.321	8.326	10.362	12.848	10.158	148.205	>0.98	2.28
151	3.70e-16	189.114756	62.205093	–	–	–	>27.800	–	>22.115	1.213	2.334	3.941	9.272	<56.234	>0.81	4.69
156	3.27e-16	189.120125	62.194539	–	–	–	>27.800	–	21.622	3.661	4.338	5.364	5.004	<56.234	>0.75	2.39
167	2.11e-16	189.130350	62.166161	28.476	27.716	27.188	26.958	22.388	20.763	9.035	10.847	14.562	14.136	196.049	0.53	3.02
181	5.65e-16	189.144062	62.161763	27.080	27.299	26.825	26.169	–	>22.188	3.531	4.351	5.819	9.510	<56.234	0.79	1.88
196	4.07e-16	189.153696	62.222391	–	–	–	>27.800	–	22.433	2.468	3.420	5.149	7.215	24.525	>0.85	3.48
198	2.54e-16	189.155634	62.110729	–	–	–	>27.800	–	21.461	7.720	8.544	10.521	6.804	<56.234	>0.64	2.08
199	2.39e-16	189.155645	62.170962	27.900	27.555	26.176	25.144	21.540	20.538	15.336	17.082	12.414	12.464	43.333	0.52	1.69
204	5.42e-16	189.162390	62.178328	–	–	–	>27.800	–	21.979	3.503	4.134	4.721	6.503	<56.234	>0.97	2.78
208	1.83e-16	189.165468	62.160321	>29.074	28.308	27.292	26.360	21.554	20.820	9.069	10.075	10.004	7.076	<56.234	0.71	2.37
220	2.76e-16	189.175460	62.225511	28.457	27.620	26.800	26.527	22.693	21.213	7.178	8.872	12.096	11.517	204.792	0.61	2.72
246	1.93e-15	189.199752	62.172370	>29.451	>29.629	28.354	27.251	21.841	21.499	6.267	7.419	6.570	4.656	<56.234	>2.26	2.80
250	1.54e-15	189.201234	62.249071	–	–	–	>27.800	–	>22.065	0.886	0.902	<2.818	<3.548	<56.234	>1.43	–
290	6.87e-16	189.235688	62.253708	–	–	–	>27.800	–	21.883	4.867	7.414	10.042	11.630	66.792	>1.08	3.30
299	5.44e-15	189.241374	62.358078	>29.896	29.285	29.181	27.782	21.674	20.583	16.511	22.039	35.778	41.371	199.074	2.57	3.65
302	1.20e-16	189.244707	62.249765	>29.965	29.518	29.233	28.096	–	21.955	7.050	9.907	10.557	9.140	117.399	1.01	2.40
307	8.76e-16	189.247128	62.309081	–	–	–	>27.800	–	21.567	8.366	10.192	14.187	21.458	271.048	>1.18	4.40
317	9.01e-17	189.256662	62.196273	>29.736	>29.892	>29.262	27.819	21.221	20.006	53.252	70.004	70.651	54.298	664.384	>1.26	1.03
321	3.97e-15	189.260124	62.323914	>29.741	28.809	28.317	27.684	–	21.656	7.486	10.640	12.880	13.057	<56.234	2.24	2.55
329	3.05e-16	189.266108	62.258594	–	–	–	>27.800	–	>22.065	0.634	0.772	<2.818	<3.548	<56.234	>0.72	–
335	1.21e-15	189.271417	62.276409	–	–	–	>27.800	22.249	22.861	2.770	3.357	4.201	6.402	<56.234	>1.32	4.60
369	3.84e-16	189.300284	62.203440	29.292	28.546	27.613	27.172	21.945	20.728	10.584	14.332	21.049	20.979	48.774	1.12	2.80
372	4.46e-16	189.306883	62.262653	–	–	–	>27.800	22.156	22.282	9.228	13.102	19.188	16.181	<56.234	>0.89	4.90
374	1.69e-15	189.307814	62.307393	–	–	–	>27.800	–	>22.069	3.490	6.133	9.344	15.957	55.452	>1.47	4.27
417	7.35e-16	189.356457	62.285502	27.678	27.280	26.292	25.779	22.512	20.886	12.484	15.920	20.284	19.973	172.580	0.90	2.44
434	8.21e-16	189.392075	62.323511	28.962	27.275	26.012	25.042	21.725	20.434	12.114	12.983	9.846	6.153	<56.234	0.94	3.39
445	4.43e-15	189.404382	62.309580	>29.544	28.945	28.249	27.339	20.903	21.146	11.426	14.165	17.488	15.500	68.500	2.34	2.52
470	1.95e-15	189.459284	62.233180	27.843	27.448	25.955	24.867	21.549	20.254	16.937	19.801	20.448	21.565	<56.234	1.39	1.67

(Civano et al. 2005) and the optically faint sample presented by Alexander et al. (2001). In Fig. 4 we plot the R magnitudes of the optical counterparts against the (0.5–8.0) keV flux as filled circles and the sources in our sample (all lower limits) as crosses. The shaded area is the $\log(f_x/f_{\text{opt}}) = 0 \pm 1$ area where the bulk of AGN are expected (e.g. Elvis et al. 1994). Our sources have, on average, a higher f_x/f_{opt} value than the bulk of the AGN population, but could not be securely considered as high f_x/f_{opt} (with a value >10 , Koekemoer et al. 2004). The *HST* V_{606} magnitudes provide a clearer picture. In Fig. 5 we plot the V_{606} magnitudes against the X-ray flux keeping the same symbols as in Fig. 4. The V_{606} magnitudes for non-detected sources are assumed to be $V_{606} > 27.8$, the same as the detection threshold in the z_{850} band. The true limits however are likely to be higher, as the typical $V_{606} - z_{850}$ colour of AGN hosts is >0.5 and increasing with redshift (Sánchez et al. 2004); the 2σ limits of sources 246 and 317, which are detected in the z_{850} band and not in the V_{606} band, are 29.6 and 29.9 respectively. In Fig. 5 we see that the sources of Table 1 are clearly relatively high f_x/f_{opt} , all having $\log(f_x/f_{\text{opt}}) > 0.52$. However, compared to Civano et al. (2005), this is neither fully a high f_x/f_{opt} sample, nor a complete one, as many sources with $\log(f_x/f_{\text{opt}}) > 1$ are not included. Moreover, the high f_x/f_{opt} sample of Civano et al. (2005) includes much brighter sources, as bright as $R \sim 23$.

Compared to Alexander et al. (2001), our sample probes much fainter sources; the Alexander et al. (2001) sample has a cut at $I = 24$. As a result, their sources have relatively low X-ray-to-optical flux ratios, in many cases $\log(f_x/f_{\text{opt}}) < 0$.

4. Photometric redshifts

We use the EAZY code (Brammer et al. 2008) to calculate photometric redshifts. We used 4 ACS (B_{435} , V_{606} , i_{775} , and z_{850}) optical, HK' (when available), K_s and 2 IRAC bands (3.6 μm , 4.5 μm) to constrain the photometric redshifts. We do not use the 5.8 μm and 8.0 μm bands because they are more sensitive to the properties of (interstellar and circumnuclear in AGN cases like here) dust, something which would add extra parameters that would have to be considered in the template fitting (see Rowan-Robinson et al. 2008).

The results are also shown in Table 1; the *HST* magnitudes shown as lower limit are detections with a $<2\sigma$ confidence in the respective bands, and the 2σ flux is used to calculate the magnitude. The photometric redshifts based on these lower limits are considered less reliable. Note that source 369, despite being very faint in the optical, has a reported spectroscopic redshift of $z = 2.914$ in Chapman et al. (2005). The position of the spectroscopic source comes from the radio (VLA – 1.4 GHz) catalogue

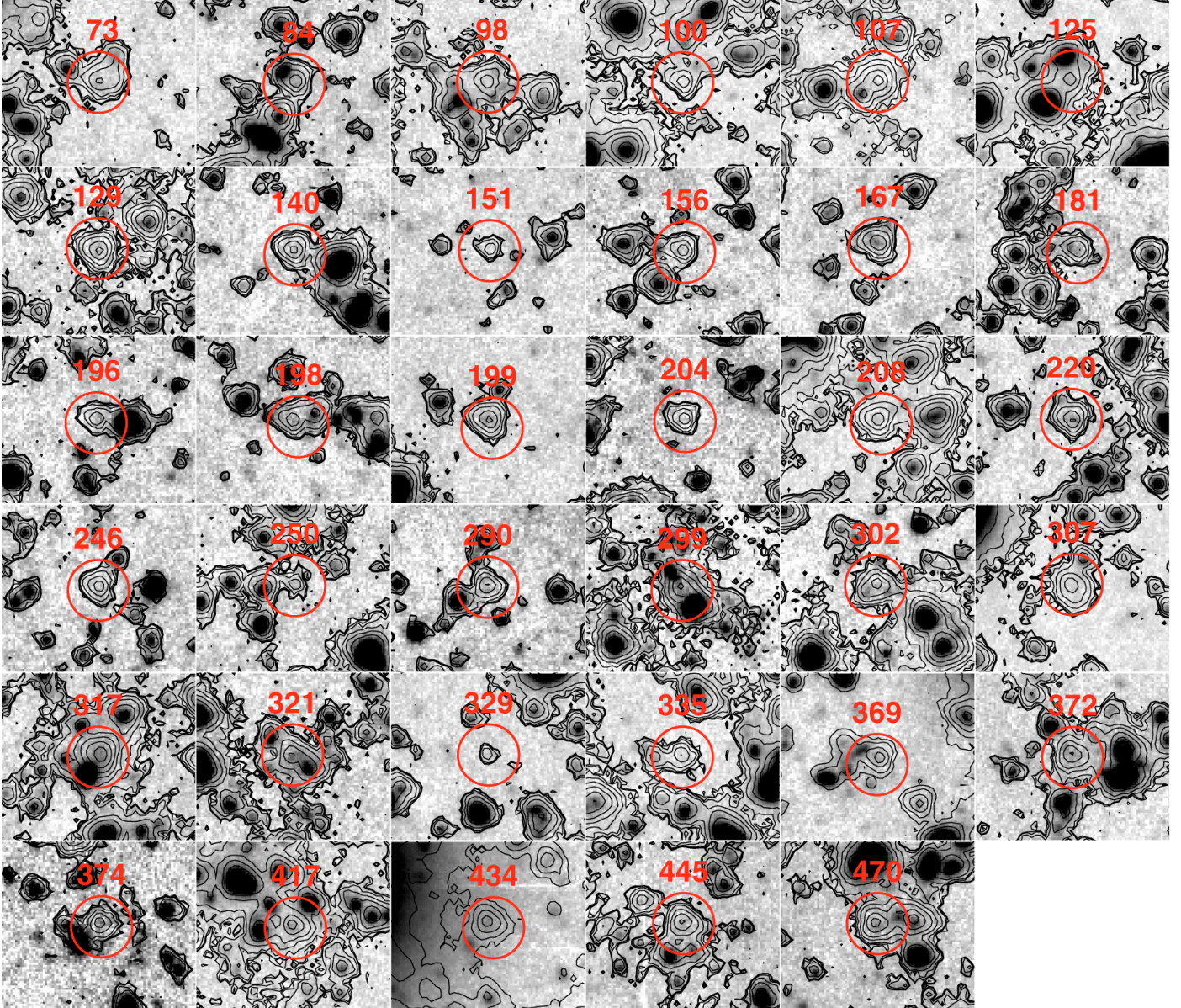


Fig. 3. Cutout images of the sources listed in Table 1. In greyscale is the Subaru *R*-band from Capak et al. (2004). Large circles mark the positions of the X-ray sources with $4''$ radii and contours represent the IRAC $3.6 \mu\text{m}$ flux. (This figure is available in color in electronic form.)

of Richards (2000) and agrees within $0.15''$ with the IRAC position. The spectrum is typical of an AGN (Civ line) and the X-ray position is $1.1''$ away, so we are confident that this is the correct counterpart. The photometric redshift derived by EAZY (2.80) is close to the spectroscopic value.

For sources without ACS detection, it is very challenging to derive a photometric redshift based only on the IRAC and K_S bands. In these cases we are forced to use all IRAC bands, which adds the extra variable of the dust properties. A good example of poor photo- z accuracy in cases where only mid-infrared fluxes are fitted can be found in Salvato et al. (2009). The redshift derived is typically $2 < z < 3$, but the constrain is weak and the broad-band spectrum in some cases can be equally well fitted with SEDs shifted to $z > 3.2$. The reason for that is that in cases where the IRAC SEDs are monotonic in f_ν , the fit cannot be easily constrained. A good photo- z estimate with a value of $z \sim 2.5$ is derived for a blue $[5.8]-[8.0]$ colour¹, which can be

¹ We define here blue as $f_{\nu, 5.8 \mu\text{m}} > f_{\nu, 8.0 \mu\text{m}}$, corresponding to $[5.8]-[8.0] < 0.64$

fitted with the red-NIR bump of a galactic (no AGN) SED due to moderate temperature interstellar gas (see Fig. 8 in Salvato et al. 2009). From Table 1, we can see that of the 14 sources with full IRAC photometry and no ACS detection, 5 have blue $[5.8]-[8.0]$ colour (98, 140, 156, 198, and 372). The median photometric redshift for these five sources as derived by EAZY is $z = 2.39$, whereas the median photo- z for the red $[5.8]-[8.0]$ colours is $z = 4.40$. The two samples define different populations in terms of photometric redshifts with a confidence level of 99.5%, according to a K-S test. Moreover, the “*HST*-detections” and “*HST*-non-detections” populations are also different within 98.9%, having median redshifts 2.61 and 3.48 respectively.

The redshift distribution of the sources in Table 1 is compared with the distribution of all X-ray sources in the common CFDFN-GOODS-MOIRCS in Fig. 6. The black histogram represents all optically detected sources and the shaded histogram represents sources with spectroscopic redshifts, taken from the catalogues of Barger et al. (2003a) and Trouille et al. (2008). The red histogram (referring to the right axis scale) represents

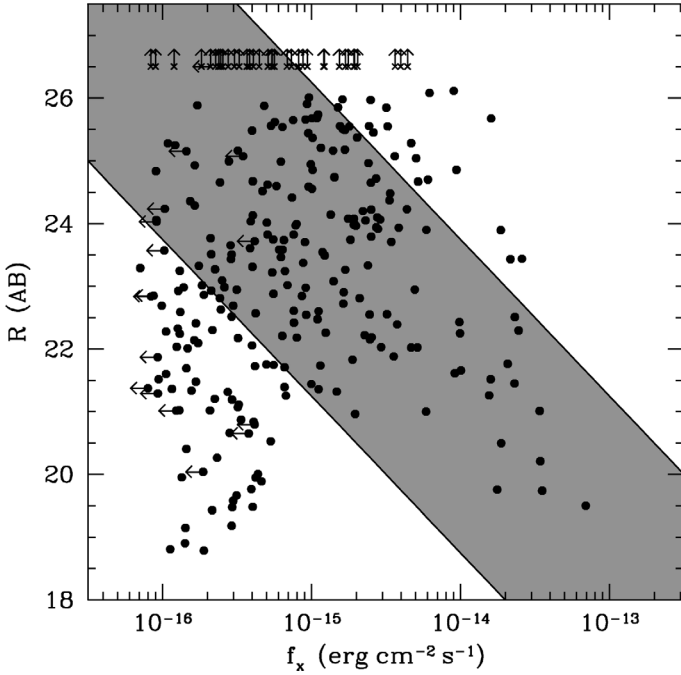


Fig. 4. Optical versus X-ray flux for all the X-ray sources in the common area (see text). Crosses mark the sources of Table 1 and the shaded area marks $\log(f_x/f_{\text{opt}}) = 0 \pm 1$ where the bulk of AGN are expected.

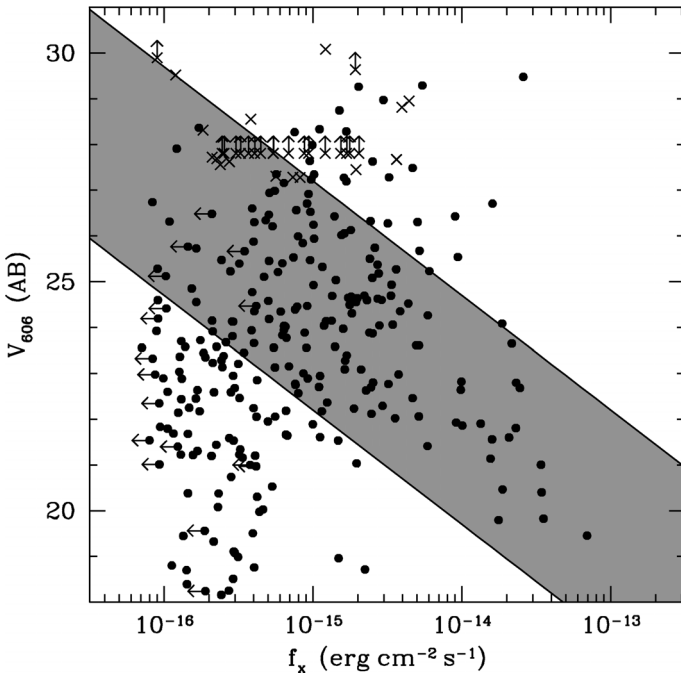


Fig. 5. Same as Fig. 4 but for the *HST*-ACS V_{606} optical flux. The $V_{606} > 27.8$ upper limit for non-detection is likely to be an under-estimation (see text).

the sources of Table 1. The two distributions are remarkably different, with the sources of Table 1 being at higher redshifts.

5. X-ray spectral analysis

The data were analysed using the CIAO v.4.1 analysis software. The source spectra were extracted from circular regions with variable radii so as to include at least 90 per cent of the source photons in all off-axis angles. There are 20 X-ray

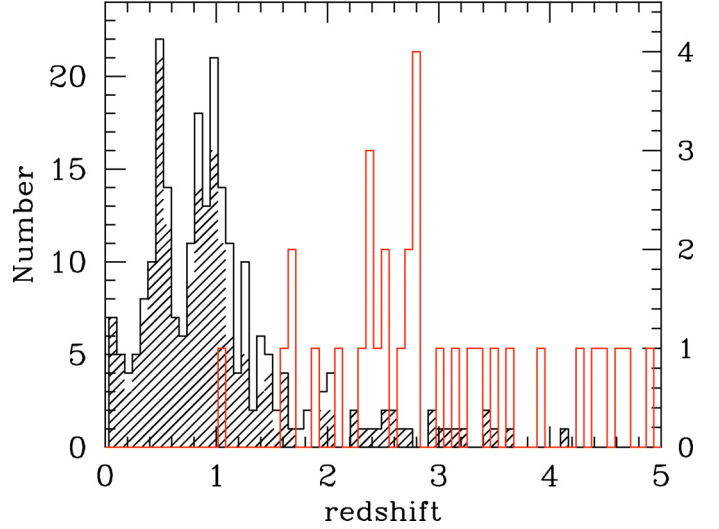


Fig. 6. Redshift distributions of CDFN sources in the common CDFN-GOODS-MOIRCS area. The black histogram represents all optically detected sources with the shaded histogram representing spectroscopic redshifts. The red histogram (referring to the right axis scale) represents the optically faint sources. (This figure is available in color in electronic form.)

observations comprising the total ~ 2 Ms exposure. We extracted the source spectrum and auxiliary files for each observation separately using the CIAO *SPEXTRACT* script. Then we used the *MATHPHA ADDARF* and *ADDRMF* tasks of *FTOOLS* to merge the spectral products for each source. The background files were calculated from source-free regions in each observation and are again merged using the *MATHPHA* tool.

We explored the X-ray properties of the 35 sources in our sample using the *XSPEC* v12.5 package to perform X-ray spectral fittings. For the sources with adequate count statistics (net source counts ≥ 200 , 5 sources), we used the χ^2 statistic technique. The data were grouped to give a minimum of 15 counts per bin to ensure that Gaussian statistics apply. We adopted an absorbed power-law model and attempted to constrain the intrinsic absorption column density N_{H} (i.e., after having subtracted the Galactic absorption) and the power-law photon index Γ .

For the sources with limited photon statistics (net counts < 200), we used the C-statistic technique (Cash 1979), which is specifically developed to extract spectral information from data with a low signal-to-noise ratio. In this case, the data are grouped to give a minimum of one count per bin to avoid zero count bins. We tried to constrain the intrinsic column densities using an absorbed power-law model with Γ fixed to 1.8. In both cases, the spectral fittings are performed in the 0.3–8 keV energy band where the sensitivity of the *Chandra* detector is the highest. The estimated errors correspond to the 90 per cent confidence level. In Table 2 we present the spectral fitting results for the 35 sources comprising our final dataset. Source 107 has a very flat photon index, which is likely to be the result of a reflection-dominated spectrum (see Georgantopoulos et al. 2009, for a detailed analysis of the candidate Compton-thick sources in the CDFN). In this case the hydrogen column density in Table 2 is not correct, and the true N_{H} of the source is $> 10^{24} \text{ cm}^{-2}$. There are two more Compton-thick sources (199 and 369) in our sample that are transmission dominated. In these the X-ray-absorption turnover is redshifted at low energies (5–6 keV) and an observer's frame $N_{\text{H}} \sim 3 \times 10^{23} \text{ cm}^{-2}$ is measured, which yields a rest-frame $N_{\text{H}} > 10^{24} \text{ cm}^{-2}$ when the $(1+z)^{2.65}$ correction is applied. The most secure Compton-thick source is 369,

Table 2. X-ray properties.

IAU	A03	Rest-frame N_{H} $\times 10^{22} \text{cm}^{-2}$	Γ	Counts	$\log(L_{2.0-10.0 \text{ keV}})$ erg s^{-1}
CXO J123605.83+620838.0	73	<1.56	$1.4^{+0.6}_{-0.4}$	175	44.00
CXO J123608.61+621435.1	84	50	1.8	20	43.61
CXO J123613.02+621224.1	98	$49.2^{+17.1}_{-12.7}$	1.8	127	44.15
CXO J123614.14+621017.7	100	$121.3^{+21.5}_{-24.3}$	1.8	56	44.07
CXO J123615.83+621515.5	107	$15.0^{+20.21}_{-12.0}$	$0.56^{+0.41}_{-0.31}$	211	44.08
CXO J123621.07+621303.3	125	$8.5^{+4.3}_{-3.5}$	1.8	33	42.53
CXO J123621.94+621603.8	129	115^{+11}_{-37}	1.8	64	44.03
CXO J123623.66+621008.7	140	$18.9^{+7.2}_{-8.4}$	1.8	69	43.33
CXO J123627.53+621218.0	151	$26.8^{+31.8}_{-19.9}$	1.8	52	43.92
CXO J123628.78+621140.0	156	$62.8^{+7.9}_{-28.5}$	1.8	42	43.27
CXO J123631.25+620957.3	167	<16.0	1.8	35	43.11
CXO J123634.48+620941.8	181	$5.8^{+5.1}_{-3.8}$	1.8	66	43.45
CXO J123636.90+621320.0	196	<298	1.8	31	43.86
CXO J123637.26+620637.5	198	$17.3^{+6.1}_{-14.2}$	1.8	46	42.91
CXO J123637.28+621014.2	199	480^{+1070}_{-460}	1.8	26	43.65
CXO J123638.94+621041.5	204	$13.2^{+8.8}_{-6.8}$	1.8	78	43.46
CXO J123639.65+620936.4	208	<25.8	1.8	27	42.88
CXO J123642.11+621331.6	220	<2.93	1.8	44	43.01
CXO J123647.94+621019.9	246	$99.7^{+12.4}_{-18.9}$	1.8	118	43.93
CXO J123648.28+621456.2	250	$1.60^{+0.902}_{-0.60}$	$2.0^{+0.7}_{-0.5}$	170	–
CXO J123656.56+621513.1	290	138^{+114}_{-50}	1.8	81	43.93
CXO J123657.91+622128.6	299	$7.05^{+2.35}_{-2.94}$	$1.71^{+0.22}_{-0.23}$	787	44.72
CXO J123658.74+621459.2	302	<159	1.8	34	42.97
CXO J123659.32+621833.0	307	$103.8^{+27.1}_{-38.4}$	1.8	67	44.21
CXO J123701.62+621146.2	317	<10.2	1.8	17	42.99
CXO J123702.43+621926.1	321	$16.37^{+2.87}_{-2.58}$	$1.92^{+0.22}_{-0.28}$	433	44.10
CXO J123703.85+621530.9	329	$1.50^{+1.502}_{-1.10}$	1.8	28	–
CXO J123705.12+621634.8	335	$67.3^{+24.0}_{-21.1}$	1.8	125	44.35
CXO J123712.09+621211.3	369	890^{+540}_{-430}	1.8	31	43.84
CXO J123713.65+621545.2	372	1380^{+1140}_{-680}	1.8	40	44.38
CXO J123713.84+621826.2	374	$31.9^{+13.1}_{-10.6}$	$2.16^{+0.48}_{-0.50}$	200	43.03
CXO J123725.50+621707.3	417	<6.3	1.8	155	43.58
CXO J123733.98+621624.0	434	90^{+43}_{-34}	1.8	27	43.44
CXO J123737.04+621834.4	445	$17.13^{+3.37}_{-2.81}$	$2.12^{+0.31}_{-0.40}$	492	44.06
CXO J123750.22+621359.3	470	170^{+100}_{-70}	1.8	105	44.16

Notes. ⁽¹⁾ Column density is more likely $>10^{24} \text{cm}^{-2}$ (see text). ⁽²⁾ *Observer's frame* column density.

for which there is spectroscopic redshift available and therefore a more reliable determination of the rest-frame column density. Note that this source is not included in the CDFN Compton-thick sample of [Georgantopoulos et al. \(2009\)](#), because it has a flux lower than their adopted flux limit of $10^{-15} \text{erg cm}^{-2} \text{s}^{-1}$ in the 2–10 keV band.

Next, we compared the mean X-ray spectral indices by coadding the individual X-ray spectra in the total 0.3–8 keV band for four different sets of sources (see Table 3). We fitted a simple power-law model to the data. It is evident that our sources present a very hard X-ray spectrum. The total spectrum of all 35 sources has $\Gamma \approx 0.9$, which is harder than the coadded spectrum of all the detected X-ray sources in this band ($\Gamma = 1.4$, [Tozzi et al. 2001](#)). Note that the derived mean spectrum is comparable to the spectrum derived by [Fiore et al. \(2008\)](#) and [Georgantopoulos et al. \(2008\)](#) for dust obscured galaxies, i.e.

sources defined as having $f_{24 \mu\text{m}}/f_R > 1000$; the coadded spectrum of DOGs in our sample has $\Gamma = 1.05$. The sources with IRAC-only detections are significantly harder than those with optical *HST* counterparts. This difference cannot be attributed to the fact that they have on average different redshifts and hence different K-corrections, as it would work in the opposite case. The *HST*-detected sources are intrinsically softer than the ones completely lacking an optical counterpart.

6. Optical properties

In Fig. 7 we plot the $V_{606} - i_{775}$ vs. $i_{775} - z_{850}$ colours of the 18 sources in our sample which have an ACS detection. Red points mark the objects of our sample and black dots are *HST* sources associated with an X-ray source. All the *HST* detections are shown in comparison as blue points. The open circle with the

Table 3. Co-added X-ray spectral properties.

Sample	No	Γ
Total	35	0.87 ± 0.05
<i>HST</i>	18	1.02 ± 0.07
IRAC-only	17	0.56 ± 0.08
DOGs	17	1.05 ± 0.06

right arrow represents source 317, which has a low significance ($<2\sigma$) detection in the V_{606} and i_{775} bands, and its $V_{606} - i_{775}$ colour cannot be accurately determined. The coloured lines in Fig. 7 trace the colours of various templates with redshift with points marking $z = 0, 1, 2, 3$. The templates are the Coleman et al. (1980) galaxy templates for elliptical, spiral, and irregular galaxies. Dotted lines correspond to $z > 4$, where the blue edge of the V_{606} filter is redshifted to the Lyman break (912 Å). The templates used are zeroed at shorter wavelengths than the Lyman break, so the dotted lines are approximations of the colours at high redshift. The sources of our sample appear significantly redder than the overall X-ray population; 55.6% (10/18) of them have $i_{775} - z_{850} > 0.8$ compared to 14.4% (42/291) of the overall X-ray population; the probability that the $i_{775} - z_{850}$ colours of the red points are a random sample of the black points in Fig. 7 is $<0.01\%$. The colours of the red objects appear to be consistent with the elliptical template at $z = 2 \pm 1$, which is backed up by the photometric redshifts of Table 1. Red optical colours are often associated with early-type morphologies (see Bell et al. 2004).

In Fig. 8 we plot the *HST*-ACS cutouts of the galaxies of Table 1. Each thumbnail is a combination of the four ACS ($B - V - i - z$) images to increase the signal-to-noise ratio, and the contours represent the IRAC 3.6 μm flux, as in Fig. 3. The crosses mark the positions of the *HST* sources with an inner radius of 0.5'' and an outer radius of 2''. We can see that for sources recovered with the *HST* the morphologies cannot be determined.

Based on their near-infrared (K_S) to optical colours, many of the sources in our sample are associated with extremely red objects (EROs; Elston et al. 1988). They are usually defined as galaxies with $R - K > 5$ (see also Alexander et al. 2002, for a selection based on the I -band with $I - K > 4$). If we use the R -band limit ($R_{AB} > 26.5 \Rightarrow R_{Vega} > 26.3$), 13/29 of the sources detected in K_S are EROs. However, the true optical flux of the sources is fainter than this limit; if we use the V_{606} ACS magnitude for *HST*-detected sources and $V_{AB} > 27.8 \Rightarrow V_{Vega} > 27.72^2$, 28/29 of the K_S detections have $V_{606} - K_S > 5$. Source 335 has $V_{606} - K_S > 4.86$ and it is not detected with the *HST*, so it is highly probable that it too is an ERO. Of the six sources not detected in K_S , 100, 151, 250, 329 and 374 are not detected with the *HST* either, so they could be associated with EROs and 181 has $V_{606} - K_S < 5.03$. Morphologically, EROs are a mix of early and late-type systems (Cimatti et al. 2003; Gilbank et al. 2003), and those with higher redshift tend to be more late-type (Moustakas et al. 2004).

7. Infrared properties

We plot the mid-infrared colours of the sources of Table 1 in Fig. 9. This diagram has been used by Stern et al. (2005) to select AGN by their mid-infrared colours; a high fraction (up to 90%)

² The detection limit in the z_{850} ACS band is 27.8(AB) and according to the colours of *HST* detections the V_{606} limit is expected to be even higher.

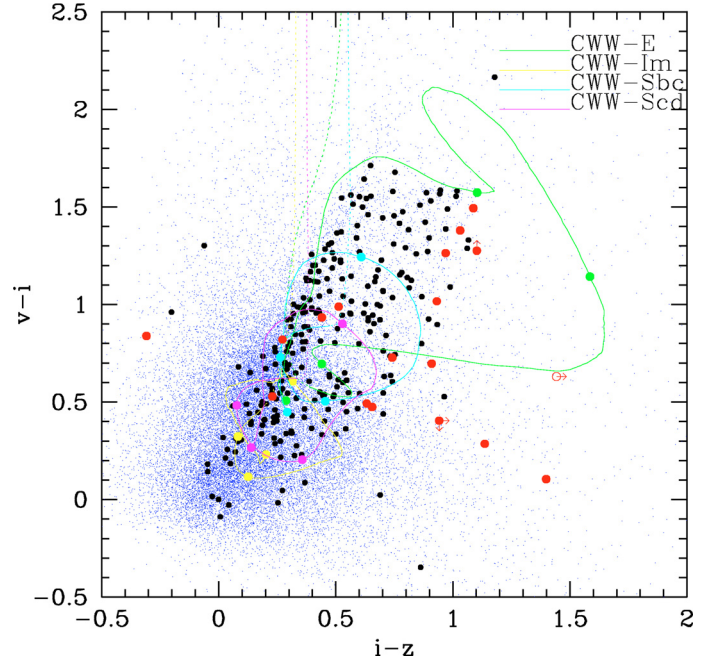


Fig. 7. Optical colours of *HST*-detected sources. The optically faint sources of Table 1 appear in red and the X-ray sources appear in black. For comparison, all *HST* sources of Giavalisco et al. (2004) are plotted in blue. Colour lines track the colours of the Coleman et al. (1980) SED templates with redshift. (This figure is available in color in electronic form.)

of broad-line AGN is located inside the “wedge” marked with the black solid line in Fig. 9. The *HST*-detected and non-detected sources of Table 1 are plotted with filled and open circles respectively. The coloured lines represent the colours of the Coleman et al. (1980) galaxy templates as well as a QSO SED (Elvis et al. 1994) for $0 < z < 8$, and point marks $z = 0, 1, 2, 3, 4, 5, 6, 7$.

The sources of Table 1 are located both inside and outside the wedge in Fig. 9, in the area where the red/optically-faint mid-IR AGN of Georgantopoulos et al. (2008) lie. There is a separation in the colours of *HST* detections and non-detections, the latter population with mid-infrared colours mostly inside the wedge (10/14), and the rest being equally distributed (9/18). This difference reflects on their [5.8]–[8.0] colours, a K-S test shows that *HST* detections have bluer [5.8]–[8.0] colours than non-detections with 99.0% (2.6 σ) significance, and this is what causes the photometric redshifts of *HST* non-detections to be higher. The galaxy templates of Coleman et al. (1980) enter the wedge at $z = 3$ so the photometric redshift of those sources is $z > 3$ if they are fitted with those templates. However, the QSO template is in the wedge independent of the redshift because of its power-law shape; indeed this is the reason why this diagram is a selection method for mid-infrared AGN. So, a red [5.8]–[8.0] colour and the position inside the wedge can be explained either with a QSO SED or a high-redshift ($z > 3$) galaxy SED.

8. Discussion

8.1. High or intermediate- z sources ?

In an earlier study of optically faint sources in the CDFN, Alexander et al. (2001) concluded that they are moderately obscured AGN at redshifts $z = 1-3$, leaving a small margin for very high redshift QSOs in the optically fainter subsample. However, their modest optical magnitude cutoff ($I > 24$) includes sources that have “normal” X-ray to optical ratios ($f_x/f_{opt} \sim 1$). Studying

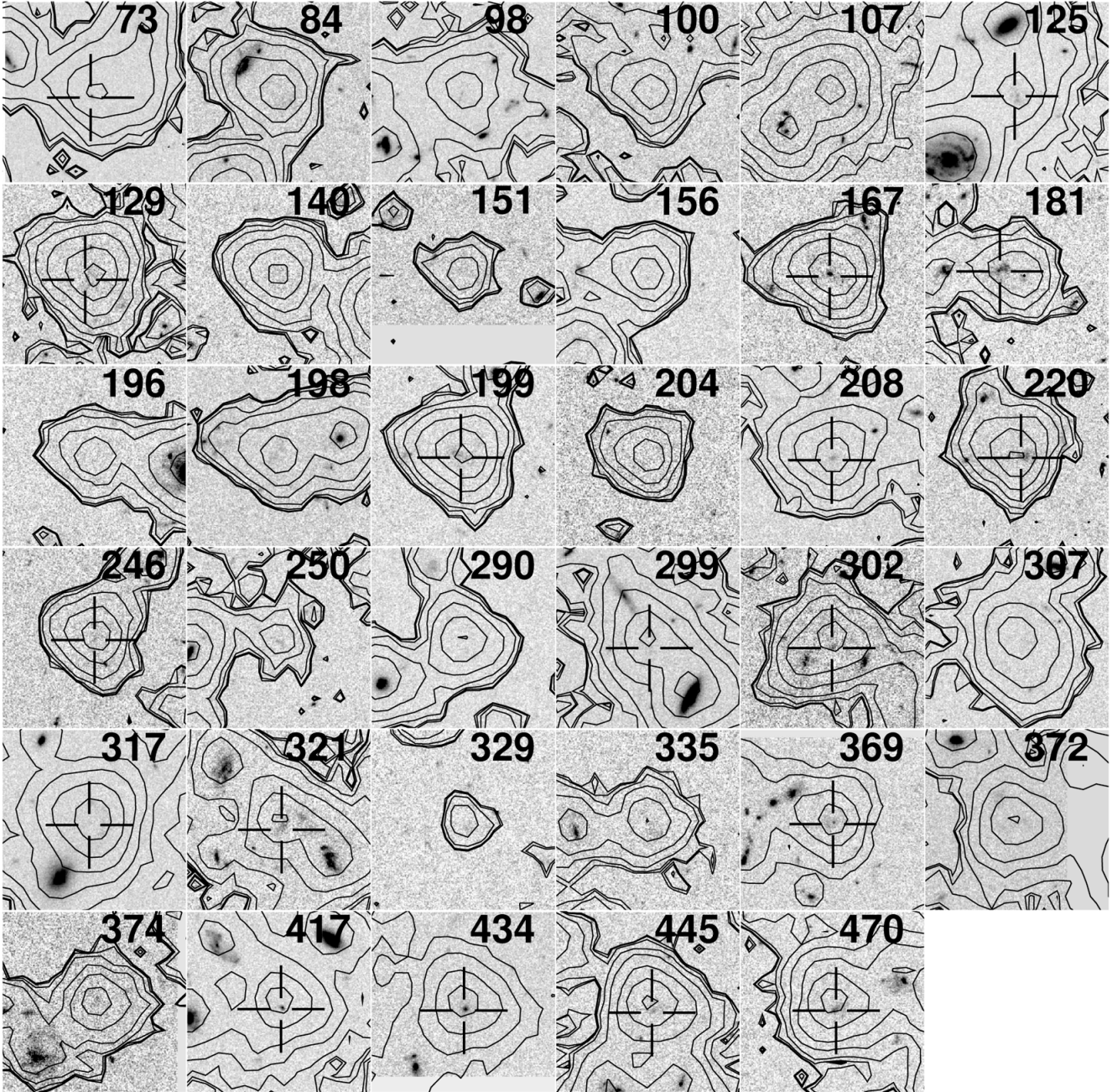


Fig. 8. *HST* cutouts of all sources listed in Table 1. The images are combinations of the four ACS bands available to increase the signal-to-noise ratio, the contours represent the IRAC flux, and the crosses are centred on the GOODS source positions (if any) with an inner radius of $0.5''$ and an outer radius of $2''$.

more extreme cases based on fainter optical fluxes or higher X-ray to optical ratios, Barger et al. (2003b) and Koekemoer et al. (2004) suggest that the existence of very high redshift objects cannot be definitely ruled out. In this study we compose a sample of the optically faintest AGN ($R > 26.5$) with robust infrared identifications which is 83.3% complete, including 35 of the 42 $R > 26.5$ X-ray sources in the common CDFN-GOODS-MOIRCS area used.

8.1.1. Multi- λ investigation

For the 18 sources with an *HST* identification we calculated their photometric redshifts using up to eight optical and infrared bands, and the results show that they are indeed at moderate redshifts, with a median $z = 2.61$, while all have $z < 3.65$.

The redshift of the remaining 17 sources without optical *HST* is harder to constrain, and we attempted to derive photometric redshifts using the infrared bands. The redshifts for sources with mid-infrared colours outside the “wedge” of Fig. 9, or alternatively with $f_{\nu 5.8 \mu\text{m}} > f_{\nu 8.0 \mu\text{m}}$ (six sources) can be better constrained, they have a median redshift of $z = 2.39$. We assume that in these cases the host galaxy dominates the mid-infrared colours, which are well fitted with non-AGN SEDs at $2 < z < 3$ (green, cyan, yellow, and magenta lines in Fig. 9). The nine sources without optical *HST* detection and $f_{\nu 5.8 \mu\text{m}} < f_{\nu 8.0 \mu\text{m}}$ have mid-infrared colours compatible both with normal galaxy (or host galaxy) templates at high redshifts or with QSO templates without a strong redshift constraint (see Sect. 4); we tried to constrain their redshifts using photometry from lower energy infrared bands ($24 \mu\text{m}$, see Soifer et al. 2008).

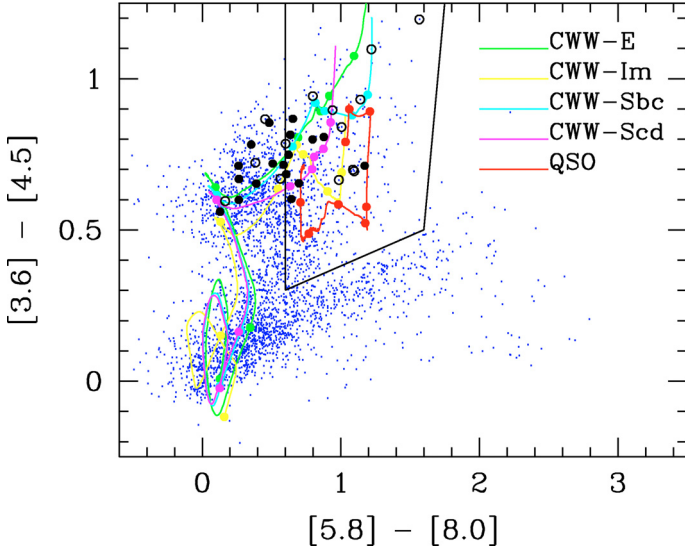


Fig. 9. Infrared colours of the sources listed in Table 1. *HST*-detected sources are plotted in filled circles and *HST* non-detections in open circles. All $3.6\ \mu\text{m}$ detected sources are plotted in blue dots. The colour lines track the colours of the Coleman et al. (1980) SED templates with redshift and the black lines mark the region where infrared-selected AGN are located (Stern et al. 2005). (This figure is available in color in electronic form.)

The position of the QSO templates inside the wedge is the result of the heating of the circumnuclear dust with the radiation of the AGN, which results in a red power-law SED ($f_\nu \propto \nu^{-\alpha}$ with $\alpha < -0.5$). The circumnuclear dust can also extinguish the optical emission; Dunlop et al. (2007) claim that optically faint sources can be well fitted with dusty and extremely reddened ($A_V \approx 4$) SEDs at moderate redshifts ($z \sim 2.5$). We therefore check the mid-infrared $24\ \mu\text{m}$ emission of the sources of our sample to examine the dust properties. Of the 17 sources without *HST* detection, seven are detected by MIPS, including 5/9 sources with $f_{\nu 5.8\ \mu\text{m}} < f_{\nu 8.0\ \mu\text{m}}$. In Fig. 10 we plot the $24\ \mu\text{m}$ emission in comparison with the $3.6\ \mu\text{m}$ emission. As dots we plot the overall population (non-AGN), as crosses we plot the counterparts of the X-ray sources (AGN) and as black filled and red open circles we plot the optically faint sources with and without an *HST* detection respectively. We can see that the optically faint sources are in general fainter in $3.6\ \mu\text{m}$ emission with respect to their $24\ \mu\text{m}$ emission, which indicates dust extinction of optical and near-infrared wavelengths, unless there is a strong $24\ \mu\text{m}$ component from the AGN. The $24\ \mu\text{m}$ emission upper limits of the *HST* non-detections can in most cases be explained with dust obscuration, in cases where $f_{3.6\ \mu\text{m}} < 5\ \mu\text{Jy}$. The harder X-ray spectra of the *HST* non-detections also suggest that (despite their somewhat higher redshifts) these sources are more obscured, and this is what causes the faint optical fluxes.

The four sources without *HST* detection, $f_{5.8\ \mu\text{m}} < f_{8.0\ \mu\text{m}}$, and no $24\ \mu\text{m}$ detection (84, 151, 204, and 335) are possibly associated with high-redshift objects. However, the $24\ \mu\text{m}$ upper limits of three of them (151, 204, and 335) do not rule out dust obscuration given their low $3.6\ \mu\text{m}$ fluxes ($< 3.6\ \mu\text{Jy}$). Source 84 with $f_{3.6\ \mu\text{m}} = 6.546\ \mu\text{Jy}$ has an $f_{3.6\ \mu\text{m}}/f_{24\ \mu\text{m}}$ ratio lower limit similar to the overall AGN population without clear signs of dust absorption and is therefore a high-redshift candidate. Its photometric redshift based on the 4 IRAC bands (4.50) is weakly constrained and not reliable.

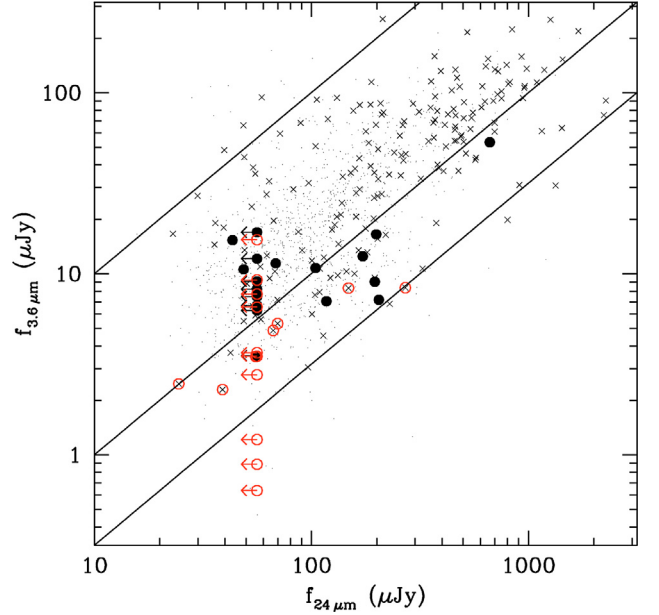


Fig. 10. $3.6\ \mu\text{m}$ vs. $24\ \mu\text{m}$ emission. Dots represent the overall $3.6\ \mu\text{m}$ population with a $24\ \mu\text{m}$ counterpart, crosses the counterparts of X-ray sources, black filled circles the sources of Table 1 detected with the *HST* and red open circles the sources of Table 1 not detected with the *HST*. The lines mark $\log(f_{3.6\ \mu\text{m}}/f_{24\ \mu\text{m}}) = 0, -1, -1.5$. (This figure is available in color in electronic form.)

8.1.2. Dropouts

The Lyman-break technique (e.g. Steidel et al. 2003) is often used to select high-redshift objects, and is based on the sudden drop in the flux of the broad-band spectrum at wavelengths smaller than $912\ \text{\AA}$. Lehmer et al. (2005) used the *HST* observations to search for dropout sources among the z_{850} -detected sources in the CDFN. They found two V_{606} -dropouts at $z \gtrsim 5$ and one i_{775} -dropout at $z \gtrsim 6$. One of the two V_{606} -dropouts (source 247 in Alexander et al. 2003) is not included in Table 1 because it is near a brighter optical source (1.6 arcsec separation) and the two are blended in the IRAC image. It has a spectroscopically confirmed redshift of $z = 5.186$ (Barger et al. 2003a). The other V_{606} -dropout (source 246) has a red $i_{775} - z_{850}$ colour (1.1), like most of the sources in the *HST*-detected sample, and its $V_{606} - i_{775}$ colour is a lower limit ($V_{606} - i_{775} > 1.275$ if we take the V_{606} 2σ limit), which is compatible both with early-type templates at $z \sim 1.5$ and with very high redshift late-type templates, depending on the true $V_{606} - i_{775}$ colour. This source is also observed spectroscopically, but neither a redshift nor a spectral type could be derived (Barger et al. 2003a; Trouille et al. 2008). It has no MIPS $24\ \mu\text{m}$ detection, but its mid-infrared colours ($[5.8] - [8.0] = 0.265$) argue against a high redshift, they are explained by normal galaxy templates with $2 < z < 3$, agreeing with the photometric redshift (2.80) derived using seven optical and infrared bands.

The i_{775} -dropout of Lehmer et al. (2005) is source 317. Its photometric redshift (3.25) is based on lower significance B_{435} , V_{606} , and i_{775} measurements and it is not reliable. This the source with the highest $24\ \mu\text{m}$ flux in our sample ($f_{24\ \mu\text{m}} = 664\ \mu\text{Jy}$), which would yield a mid-infrared luminosity of the order of $10^{26}\ \text{W Hz}^{-1}$ in the $3.5\ \mu\text{m}$ rest-frame band if the source were lying at $z \sim 6$. Its low $f_{3.6\ \mu\text{m}}/f_{24\ \mu\text{m}}$ ratio however ($10^{-1.1}$) implies dust obscuration according to Fig. 10, making it more likely to be optically faint as a result of obscuration rather than high redshift.

The dropout technique is proposed to select high-redshift objects, but it is based in 2–3 bands, usually including upper limits. All sources in our sample are “optical dropouts” in the sense that they are not detected in wavelengths shorter than a limit, in this case the *R*-band optical, and taking the *HST* observations into account, almost half of them are *z*-dropouts. When considering their multi-band properties however we see that a small fraction of them (if any) can be high-redshift ($z \gtrsim 6$) sources, as there are other processes which can cause the faint optical fluxes. Because the SEDs are a combination of the AGN and the host galaxy, a simple colour selection could be misleading in our examination of AGN-hosting systems

8.2. Obscured AGN?

The colour-colour diagram of Fig. 7 shows that the sources that are detected by the *HST* have on average redder optical colours than the overall X-ray population and are compatible with elliptical galaxy SEDs. Rovilos & Georgantopoulos (2007) and Georgakakis et al. (2008) have shown that red-cloud AGN are obscured post-starburst systems. Instead, Brusa et al. (2009) attribute the red colours to dust-reddening rather than to an evolved stellar population. It is still true though that X-ray AGN with red optical colours have a high fraction of obscured sources.

A number of studies (e.g. Alexander et al. 2001; Mignoli et al. 2004; Koekemoer et al. 2004) relate high X-ray-to-optical ratios to the extremely red objects sample, with $R - K > 5$. The sources of Table 1 have by definition high X-ray-to-optical ratios. Using the *HST* magnitudes, we get $\log(f_x/f_{\text{opt}}) > 0.52$ between the ACS-*V* band ($\lambda_{\text{eff}} = 6060 \text{ \AA}$) and the (0.5–10) keV X-ray band, assuming an optical limit $V_{606} > 27.8$ (AB) for non detected sources (see Sect. 3 and Fig. 5). They also have very red colours with $V_{606} - K_S > 5$. X-ray detected EROs are assumed to be low-Eddington obscured AGN and they show on average high f_x/f_{opt} values (Brusa et al. 2005), like our sources. The *HST*-detected subsample, which shows red optical colours, has similar characteristics to the high X/O EROs of Mignoli et al. (2004), although this is a much fainter sample. Their sample is detected in the *K*-band and has bulge-dominated morphologies, dominated by their host galaxies (see also Maiolino et al. 2006).

The sources in our sample are selected to have faint optical fluxes, and thus naturally many of them are associated with DOGs. They are found at a redshift of $z \simeq 2$ (e.g. Pope et al. 2008) and are thought to be marking a phase of bulge and black-hole growth. Hydrodynamic simulations (Narayanan et al. 2010) suggest that DOGs are rapidly evolving from starburst to AGN-dominated systems through mergers in cases where $f_\nu(24 \mu\text{m}) \gtrsim 300 \mu\text{Jy}$. Alternatively, in cases where $f_\nu(24 \mu\text{m}) \lesssim 300 \mu\text{Jy}$ the evolution is secular, that is through smaller gravitational perturbations. Their morphological characteristics (Melbourne et al. 2009) reveal less concentrated systems for lower luminosities.

Considering the V_{606} magnitudes, and a $V_{606} > 27.8$ in cases of *HST* non-detections, all objects in Table 1 with a MIPS detection (17/35 sources) have DOG characteristics³, and based on $24 \mu\text{m}$ upper limits the rest are not incompatible with DOGs, as the $f_\nu(24 \mu\text{m})/f_\nu(V_{606})$ upper limit is always > 1250 . Therefore half of our sample have characteristics consistent with DOGs and this is only a lower limit. Only one source (317) has $f_\nu(24 \mu\text{m}) > 300 \mu\text{Jy}$. Their red optical colours (*HST* detections) suggest early-type bulge-dominated morphologies (Bell et al. 2004; Mignoli et al. 2004), although the morphologies cannot

³ They all have $f_\nu(24 \mu\text{m})/f_\nu(V_{606}) > 1000$, except source 196 with $f_\nu(24 \mu\text{m})/f_\nu(V_{606}) > 890$.

be determined from direct observations, which is in line with their low $24 \mu\text{m}$ fluxes (see also Busmann et al. 2009). In conjunction with the obscured nature of the AGN, this means that the host galaxy is dominating the optical light.

On the basis of an X-ray stacking analysis in deep X-ray fields, Fiore et al. (2008, 2009); Treister et al. (2009) propose that DOGs may be hosting a large fraction of Compton-thick sources (see also Georgantopoulos et al. 2008). The sources of our sample appear to be more obscured than the overall X-ray population, the average spectral index being $\Gamma = 0.87$ compared to $\Gamma = 1.4$ (Tozzi et al. 2001). The stacked spectrum of X-ray detected DOGs in the *Chandra* deep fields is $\Gamma \simeq 0.7$ (Georgantopoulos et al. 2008), comparable to those of our total and DOG samples. The average Γ of our DOG sample is very close to the value derived by Georgantopoulos et al. (2010, submitted) using all DOGs in the CDFN regardless of their optical detection (or lack of it), a sample broadly overlapping with ours.

According to Table 2, the average column density is a few times 10^{23} cm^{-2} . A few Compton-thick AGN may be also present in our sample, this includes the reflection-dominated source (107; see Georgantopoulos et al. 2009). Two more “mildly” Compton-thick sources, i.e. with column densities $N_{\text{H}} \sim 10^{24} \text{ cm}^{-2}$, are directly identified on the basis of their absorption turnover entering the *Chandra* passband. Finally, we note that a number of our sources (10/35) of Table 2 have unobscured hard X-ray luminosities $L_x > 10^{44} \text{ erg s}^{-1}$ and intrinsic $N_{\text{H}} > 10^{23} \text{ cm}^{-2}$, making them members of the QSO2 class. It is interesting that these sources do not reveal their QSO nature except in X-rays.

8.3. X-ray luminosity function incompleteness

In the CDFs a number of X-ray sources lack an optical counterpart, even in the deepest ground-based optical surveys. More specifically, within the common CDFN – GOODS – MOIRCS area there are 35 sources which are not detected at a magnitude limit of $R \sim 26.5$ and 17 sources not detected at $z_{850} \sim 27.8$. These populations represent 11.3% and 5.5% of the X-ray population detected in this area. These numbers should be considered as lower limits, as there are seven other X-ray sources without optical counterpart not included in Table 1 because either they are not detected with *Spitzer* or have unreliable photometry. Moreover, there is a number of stars, normal galaxies, or ultraluminous X-ray sources (Hornschemeier et al. 2003; Bauer et al. 2004) among the 310 X-ray sources, so the fraction of non-optically identified X-ray AGN is even higher.

This sample of optically faint X-ray sources is not random in their redshift distribution; the redshifts calculated in Sect. 4 and the K-S test performed show that the optically faint X-ray sources have significantly higher redshifts than the overall population and the *HST* non-detections higher again. The redshifts listed in Table 1 are in 34/35 cases higher than 1.5. There are 41 sources if we count the sources within the common GOODS – IRAC – MOIRCS area with an optical detection in Capak et al. (2004) and $z > 1.5$. This means that the incompleteness of the X-ray $z > 1.5$ population with an optical identification and a redshift estimation is $\sim 50\%$ and it becomes even higher at higher redshifts; 29/35 of our sources have $z > 2$.

This has implications in the calculation of the X-ray luminosity function at high redshift ($z > 2-4$) and its evolution (e.g. Silverman et al. 2008; Aird et al. 2008; Yencho et al. 2009; Aird et al. 2010). More specifically, this incompleteness affects the faint end of the XLF, as its “knee” at $z = 2$ is at $\log L_x \sim 44.5 \text{ erg s}^{-1}$ ($\log L_* = 44.4-45.0 \text{ erg s}^{-1}$ depending on the luminosity evolution model, Silverman et al. 2008;

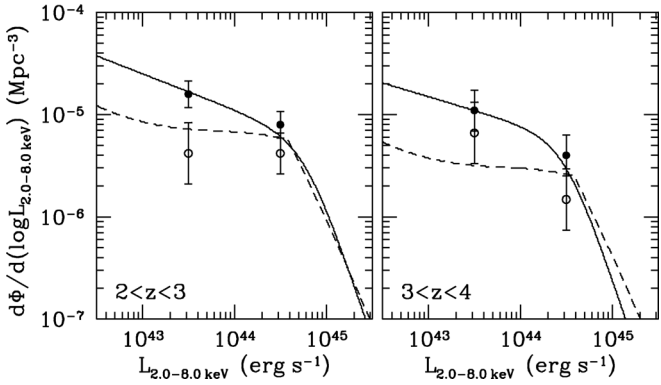


Fig. 11. Space density of AGN in the CDFN in two redshift bins ($2 < z < 3$, left, and $3 < z < 4$, right) and two luminosity bins ($10^{43} < L_{2.0-8.0\text{keV}} < 10^{44}$, and $10^{44} < L_{2.0-8.0\text{keV}} < 10^{45}$), without correction applied for optical non-detections. Open symbols are based on the sources in the CDFN – GOODS – MOIRCS area with a redshift determination in Barger et al. (2003a) and Trouille et al. (2008) and filled symbols are based on the combination of those sources with those of Table 1. The solid and dashed lines represent the best-fit mod-PLE and LDDE models respectively (see Silverman et al. 2008).

Aird et al. 2010), and 34/35 of the sources in Table 2 have unobscured X-ray luminosities $L_x < 10^{44.5}$ erg s⁻¹ in the 2–8 keV band.

In order to test how the inclusion of the sources in Table 1 affects the luminosity function at high redshift, we calculate the luminosity function of AGN in two redshift bins, $2 < z < 3$, and $3 < z < 4$, with and without their contribution, using the method described by Page & Carrera (2000). We used the combination of the CDFN catalogues of Barger et al. (2003a) and Trouille et al. (2008) and selected sources in the combined CDFN – GOODS – MOIRCS area. We did not make any distinction between spectroscopic and photometric redshifts and we do not correct for optically unidentified sources. This has an effect on the derived luminosity function only when we do not include the sources of Table 1, as the final sample is nearly complete.

The result is plotted in Fig. 11. We can see that the inclusion of the new sources severely affects the calculated luminosity function. We note that in most cases in the literature the incompleteness caused by optically non-detected sources is treated by either taking an optically bright sample which is spectroscopically complete, with the side effect of undersampling the high redshift – low luminosity cases (e.g. Yenko et al. 2009), or using simplistic assumptions, like that their redshift distribution is directly connected to their X-ray flux (e.g. Silverman et al. 2008), which is generally not true, or treating the incompleteness as a free parameter when fitting the datapoints to determine the luminosity function evolution (e.g. Aird et al. 2010). In Fig. 11 we also compare our datapoints with models of AGN evolution, which we adopt from Silverman et al. (2008). These are a modified pure luminosity evolution (mod-PLE) model (see Hopkins et al. 2007) (solid line) and a luminosity-dependent density evolution (LDDE) model (dashed line). Our datapoints are remarkably close to the prediction of the mod-PLE model, while the non-corrected points are closer to those of the LDDE model. A thorough investigation of the luminosity function evolution however would require taking into account sources at all redshifts and luminosities, which would vastly increase the reliability of the statistics. This analysis is beyond the scope of this work, but we caution that the optically faint sources, despite being a small minority of the X-ray sources, can impact the LF in high redshifts because of their redshift distribution.

9. Conclusions

We have examined the mid-IR and X-ray properties of 35 X-ray-selected sources in the GOODS-N area that are optically faint ($R_{AB} > 26.5$) and therefore missed in ground-based optical observations. Instead of relying on previous work on the matching between X-ray and optical counterparts, our sample has been compiled anew. We found secure $3.6 \mu\text{m}$ counterparts for the X-ray sources using a likelihood-ratio technique, and then we searched for their possible optical ground-based R_{AB} counterparts. Where there were none down to $R_{AB} = 26.5$, we searched for *HST* ACS optical counterparts. Eighteen sources have *HST* counterparts, while the remaining have no optical counterparts. Our findings can be summarized as follows:

1. Our sources populate moderate to high redshifts, while they are at markedly different redshifts from the already spectroscopically identified population, which peaks at $z \sim 0.7$. In particular, the redshifts of the AGN with *HST* detections have moderate values with a median redshift of 2.6. The redshifts of the sources with IRAC detections only are definitely more uncertain; the objects with blue [5.8]–[8.0] colours are probably located at redshifts comparable with the *HST* population, $z \sim 2.5$, while the remaining sources could lie at $z \gtrsim 3.2$. A couple of *V* and *i* dropouts exist in our sample (previously reported by Lehmer et al. 2005), we however propose that they are moderate redshift ($z = 2-3$) dust-extinguished AGN, rather than lying at very high redshift ($z > 5$).
2. The sources without optical counterparts in deep ground-based optical surveys constitute a large fraction (>50%) of the total source population at high redshift ($z > 2$). This has important implications for the calculation and modelling of the luminosity function at high redshift, which in the case of our highly complete sample (97% of the X-ray sources have spectroscopic or photometric redshifts) is better represented by a modified PLE model.
3. Our sources present very red colours. In particular, all 35 sources with available K_S magnitudes would be characterized as EROs on the basis of their $V_{606} - K_S$ colour.
4. The mid-IR colours of the sources with *HST* counterparts lie outside the AGN wedge in a region occupied by $z \sim 2$ galaxies according to the galaxy templates, and have blue [5.8]–[8.0] colours. The majority *Spitzer* IRAC mid-IR colours of the remaining sources without optical counterparts lie within the AGN “wedge”, suggesting either QSO templates or galaxy templates at high redshift ($z > 3$).
5. We find four high-redshift candidates based on their non-detection with the *HST*, red [5.8]–[8.0] colour, and non-detection with MIPS at $24 \mu\text{m}$. However, the low IRAC $3.6 \mu\text{m}$ of three of them do not definitely rule out dust obscuration in optical wavelengths.
6. Seventeen out of 35 sources are detected in $24 \mu\text{m}$ and can be classified as optically faint mid-IR bright galaxies. This class of objects is widely believed to consist of reddened sources at moderate (~ 2) redshifts.
7. The mean X-ray spectrum of our sources is very hard with $\Gamma \approx 0.9$, much harder than the spectrum of all sources in the CDFs, suggesting that we are viewing heavily obscured sources. The X-ray spectroscopy of the individual sources suggests that three sources are candidate Compton-thick AGN.

Obviously the current deepest X-ray observations are not at par with the present day optical spectroscopic capabilities. *Spitzer*

has detected the faintest X-ray sources and thus provided aid in the determination of their properties and photometric redshifts.

Acknowledgements. I.G. acknowledges the receipt of a Marie Curie Fellowship Grant. The data used here have been obtained from the *Chandra* X-ray archive, the NASA/IPAC Infrared Science Archive and the MAST multimission archive at StScI.

References

- Aird, J., Nandra, K., Georgakakis, A., Laird, E. S., et al. 2008, *MNRAS*, 387, 883
- Aird, J., Nandra, K., Laird, E. S., et al. 2010, *MNRAS*, 401, 2531
- Alexander, D. M., Brandt, W. N., Hornschemeier, A. E., et al. 2001, *AJ*, 122, 2156
- Alexander, D. M., Vignali, C., Bauer, F. E., et al. 2002, *AJ*, 123, 1149
- Alexander, D. M., Bauer, F. E., Brandt, W. N., et al. 2003, *AJ*, 126, 539
- Barger, A. J., Cowie, L. L., Capak, P., et al. 2003a, *AJ*, 126, 632
- Barger, A. J., Cowie, L. L., Capak, P., et al. 2003b, *ApJ*, 584, L61
- Bauer, F. E., Alexander, D. M., Brandt, W. N., et al. 2004, *AJ*, 128, 2048
- Bell, E. F., McIntosh, D. H., Barden, M., et al. 2004, *ApJ*, 600L, 11
- Bertin, E., & Arnouts, S. 1996, *A&AS*, 117, 393
- Brandt, W. N., & Hasinger, G. 2005, *ARA&A*, 43, 827
- Bundy, K., Fukugita, M., Ellis, R. S., et al. 2009, *ApJ*, 697, 1369
- Bussmann, R. S., Dey, A., Lotz, J., et al. 2009, *ApJ*, 693, 750
- Brammer, G. B., van Dokkum, P. G., & Coppi, P. 2008, *ApJ*, 686, 1503
- Brusa, M., Comastri, A., Daddi, E., et al. 2005, *A&A*, 432, 69
- Brusa, M., Fiore, F., Santini, P., et al. 2009, *A&A*, 507, 1277
- Capak, P., Cowie, L. L., Hu, E. M., et al. 2004, *AJ*, 127, 180
- Cash, W. 1979, *ApJ*, 228, 939
- Chapman, S. C., Blain, A. W., Smail, I., & Ivison, R. J. 2005, *ApJ*, 622, 772
- Ciliegi, P., Zamorani, G., Hasinger, G., et al. 2003, *A&A*, 398, 901
- Civano, F., Comastri, A., & Brusa, M. 2005, *MNRAS*, 358, 693
- Cimatti, A., Daddi, E., Cassata, P., et al. 2003, *A&A*, 412, L1
- Coleman, G. D., Wu, C.-C., & Weedman, D. W. 1980, *ApJS*, 43, 393
- Dickinson, M. 2004, *BAAS*, 36, 1614
- Giavalisco, M., Ferguson, H. C., Koekemoer, A. M., et al. 2004, *ApJ*, 600, L93
- Gilbank, D. G., Smail, I., Ivison, R. J., & Packham, C. 2003, *MNRAS*, 346, 1125
- Daddi, E., Alexander, D. M., Dickinson, M., et al. 2007, *ApJ*, 670, 173
- Dey, A., Soifer, B. T., Desai, V., et al. 2008, *ApJ*, 677, 956
- Dunlop, J. S., Cirasuolo, M., & McLure, R. J. 2007, *MNRAS*, 376, 1054
- Elston, R., Rieke, G. H., & Rieke, M. J. 1988, *ApJ*, 331, L77
- Elvis, M., Wilkes, B. J., McDowell, J. C., et al. 1994, *ApJS*, 95, 1
- Fiore, F., Grazian, A., Santini, P., et al. 2008, *ApJ*, 672, 94
- Fiore, F., Puccetti, S., Brusa, M., et al. 2009, *ApJ*, 693, 447
- Georgakakis, A., Nandra, K., Yan, R., et al. 2008, *MNRAS*, 385, 2049
- Georgantopoulos, I., Georgakakis, A., Rowan-Robinson, M., & Rovilos, E. 2008, *A&A*, 484, 671
- Georgantopoulos, I., Akylas, A., Georgakakis, A., & Rowan-Robinson, M. 2009, *A&A*, 507, 747
- Hopkins, P. F., Richards, G. T., & Hernquist, L. 2007, *ApJ*, 654, 731
- Hornschemeier, A. E., Bauer, F. E., Alexander, D. M., et al. 2003, *AJ*, 126, 575
- Houck, J. R., Soifer, B. T., Weedman, D., et al. 2005, *ApJ*, 622, L105
- Kalberla, P. M. W., Burton, W. B., Hartmann, D., et al. 2005, *A&A*, 440, 775
- Koekemoer, A. M., Alexander, D. M., Bauer, F. E., et al. 2004, *ApJ*, 600, L123
- Lehmer, B. D., Brandt, W. N., Alexander, D. M., et al. 2005, *AJ*, 129, 1
- Luo, B., Bauer, F. E., Brandt, W. N., et al. 2008, *ApJS*, 179, 19
- Luo, B., Brandt, W. N., Xue, Y. Q., et al. 2010, *ApJS*, 187, 560
- Mainieri, V., Rosati, P., Tozzi, P., et al. 2005, *A&A*, 437, 805
- Maiolino, R., Mignoli, M., Pozzetti, L., et al. 2006, *A&A*, 445, 457
- Melbourne, J., Bussmann, R. S., Brand, K., et al. 2009, *AJ*, 137, 4854
- Mignoli, M., Pozzetti, L., Comastri, A., et al. 2004, *A&A*, 418, 827
- Moustakas, L. A., Casertano, S., Conselice, C. J., et al. 2004, *ApJ*, 600, L131
- Narayanan, D., Dey, A., Hayward, C., et al. 2010, *MNRAS*, 407, 1701
- Page, M. J., & Carrera, F. J. 2000, *MNRAS*, 311, 433
- Pope, A., Bussmann, R. S., Dey, A., et al. 2008, *ApJ*, 689, 127
- Richards, E. A. 2000, *ApJ*, 533, 611
- Rovilos, E., & Georgantopoulos, I. 2007, *A&A*, 475, 115
- Rowan-Robinson, M., Babbedge, T., Oliver, S., et al. 2008, *MNRAS*, 386, 697
- Salvato, M., Hasinger, G., Ilbert, O., et al. 2009, *ApJ*, 690, 1250
- Sánchez, S. F., Jahnke, K., Wisotzki, L., et al. 2004, *ApJ*, 614, 586
- Silverman, J. D., Green, P. J., Barkhouse, W. A., et al. 2008, *ApJ*, 679, 118
- Soifer, B. T., Helou, G., & Werner, M. 2008, *ARA&A*, 46, 201
- Steidel, C. C., Adelberger, K. L., Shapley, A. E., et al. 2003, *ApJ*, 592, 728
- Stern, D., Eisenhardt, P., Gorjian, V., et al. 2005, *ApJ*, 631, 163
- Sutherland, W., & Saunders, W. 1992, *MNRAS*, 259, 413
- Tozzi, P., Rosati, P., Nonino, M., et al. 2001, *ApJ*, 562, 42
- Treister, E., Cardamone, C. N., Schawinski, K., et al. 2009, *ApJ*, 706, 535
- Trouille, L., Barger, A. J., Cowie, L. L., Yang, Y., & Mushotzky, R. F. 2008, *ApJS*, 179, 1
- Yencho, B., Barger, A. J., Trouille, L., & Winter, L. M. 2009, *ApJ*, 698, 380